Computational Materials Science 129 (2017) 98–106

Contents lists available at ScienceDirect

Computational Materials Science

journal homepage: www.elsevier.com/locate/commatsci

Simulations of cratering and sputtering from an ion track in crystalline and amorphous Lennard Jones thin films

L.I. Gutierres [a], N.W. Lima [a], R.S. Thomaz [a], R.M. Papaléo [a], E.M. Bringa [b]

[a] Faculdade de Física, Pontifícia Universidade Católica do Rio Grande do Sul, Av. Ipiranga 6681, 90619-900 Porto Alegre, Brazil
[b] CONICET and Facultad de Ciencias Exactas y Naturales, Universidad Nacional de Cuyo, Mendoza 5500, Argentina

ARTICLE INFO

Article history:
Received 19 July 2016
Received in revised form 29 November 2016
Accepted 2 December 2016
Available online 27 December 2016

Keywords:
Molecular dynamics simulations
Swift heavy ions
Craters
Polymers

ABSTRACT

Impacts of swift heavy ions of different energy loss in amorphous and crystalline Lennard-Jones (LJ) thin films (2–60 nm) were simulated using classical molecular dynamics to study cratering and sputtering in model molecular thin films. Crater size is determined mostly by evaporation and melt flow from the hot ion track, while rim size is determined both by melt flow and by coherent displacement of particles due to the large pressure developed in the excited region, with minor influence of particles from the substrate. Sputtering yields from both crystalline and amorphous samples are similar (including the scaling with energy loss), due to the extremely high temperature and disordered condition of the track region from where most ejected particles originate in the early stages of the track evolution. Cratering, however clearly depends on the crystallinity of the film. Craters and rims are much smaller in crystalline films mainly due to faster energy dissipation, higher stress threshold for plasticity and smaller free-volume in the ordered phase. We also found a large dependence of the induced surface effects on film thickness below a critical thickness value. The pressure pulse due to the ion impact is weaker and cooling of the excited track is more efficient in short tracks, both contributing to the decreased radiation damage efficiency on ultrathin layers. Despite the simplicity of the LJ model, the simulations in the amorphous films reproduce remarkably well several of the experimental features seen recently on polymer thin and ultrathin films irradiated by swift heavy ions.

1. Introduction

Swift heavy ions (SHI) penetrating solids lead to extreme levels of highly localized electronic excitations, which may produce damage tracks [1–3], electronic sputtering [4,5], phase transitions [6], cratering [7,8] and other topographic features [9–11]. Such effects have been widely explored to tailor materials properties in a broad spectrum of technological applications. Even if the initial excitation state was known, the subsequent non-equilibrium processes leading to lasting material modification have time scales from femtoseconds to microseconds and are poorly understood. This problem has been treated from many different theoretical viewpoints. There are thermal spike models that focus on thermal effects [12–14], including various two temperature models [2,15]. There are also models which focus on pressure effects alone [16], and models where modification is produced above a critical energy [17] or energy density/pressure, like the pressure pulse model [18]. However, the presence of a surface, together with phase transitions and transport properties that depend on temperature and density make the quantitative applicability of these models problematic, as Jakas et al. [19] showed, by solving the full set of fluid dynamics equations for this problem.

As an alternative to semi-analytical models, molecular dynamics simulations (MDS) of thermal spikes and two temperature models have proven useful to model complex effects in bulk materials [20], and materials with an "infinite surface" [21]. Classical MD simulations can use heating models to include the role of electronic excitations and help to explain experimental results on track radii [20,22,23], sputtering yields [12,18,24,25], and crater sizes [26,27] in different materials, from frozen gases and inorganic solids to complex organic compounds or nanoparticles [28]. In particular, MDS of a Lennard-Jones material were able to obtain qualitative agreement with experiments of cratering in polymers, including the dependence of crater size with ion velocity and angle of incidence [27]. Recently, this model was used to fit data in a study of confinement effects of ion tracks in thin polymer films [25] in which radiation effects at the surface were shown to be size-dependent below a critical thickness.

In this work, simulations on SHI irradiation of ultrathin LJ films are described in detail. Some preliminary results were presented in

http://dx.doi.org/10.1016/j.commatsci.2016.12.001
0927-0256/

Ref. [25]. We first analyze and compare crater formation and particle ejection from amorphous and crystalline samples, including temperature effects and the relevance of the different mechanisms involved. In a second part, we focus on film thickness effects on cratering and sputtering, comparing MDS results to recent experiments in poly(methyl methacrylate) (PMMA). The simulated results present very good qualitative agreement with the experimental data.

2. Simulation methods

Molecular dynamics simulations were carried out with LAMMPS [29] at the computer cluster of the Laboratory of High Performance (LAD), PUCRS. Although there are several ways to mimic electronic excitations in classical MD simulations [18,20,28], the present simulations were mostly motivated by experiments on thin polymer films, and were carried out as previously done for "bulk" polymers [27]. Polymer molecules were simply modeled assuming each monomer is a particle ($m = 1.66 \times 10^{-22}$ g, as in a PMMA monomer) interacting via a Lennard-Jones (LJ) potential with parameters $\sigma = 0.5$ nm, $\varepsilon = 0.07$ eV and cut-off radius of 2.5σ. The time in reduced LJ units t_{LJ} scales with the mass (m), σ, and ε, via $t_{LJ} = \sigma(m/\varepsilon)^{1/2} \sim 1.9ps$. The timestep command was set to $0.001t_{LJ}$.

We simulated both crystalline and amorphous LJ samples, although experimental results are available only for amorphous polymers. This was done to investigate the effect of structural order in the response of a LJ thin film to an ion track, an issue not yet considered in the literature, despite the common use of the LJ potential in simulations of radiation effects. Crystalline samples were built with a face centered cubic (fcc) structure, and a [001] surface as in most previous studies [21,27,30]. Amorphous samples were obtained following the methodology described in Ref. [28]. Tracks in amorphous LJ systems have been simulated previously, but for nanoparticles [28] not films, except for the preliminary results in [25]. Simulation boxes were centered at the origin and had both top and bottom free surfaces perpendicular to the z-axis. All other surfaces include a region of Langevin thermostating and damping with thickness 2σ. Periodic boundary conditions were applied in xy directions. Simulated targets had about 4 million particles, which was enough to avoid significant boundary effects for the track sizes and temperatures used. In some cases, 2–5 simulations were carried out for the same irradiation condition, and the resulting standard deviation in feature sizes was always less than 15%, and smaller than experimental uncertainties.

To model the ion track produced by normal incidence, molecules within a cylinder of radius $R_{track} = 2–8\sigma$ (1–4 nm) centered near (x,y) = (0,0) were given an energy distribution with 3/2 kT = 5–50ε (or track temperatures in reduced units T^* from 5 to 50), over a time of 0.2 t_{LJ}. The energy deposited along the ion path which was effectively transferred into atomic motion - the $(dE/dx)_{eff}$ - was calculated from the total mechanical energy input into the system by this temperature increase, divided by the length of the track (which is equal to the film thickness). The $(dE/dx)_{eff}$ values obtained scaled linearly with T^*. The relationship between the simulated and the experimental value of the electronic energy loss $(dE/dx)_{el}$ is not straightforward, since there are several possible channels for excitation decay, which may not be related to crater formation and sputtering. We assume a simple proportionality relationship, where both are connected by an efficiency parameter α, often taken to be around 0.2, i.e. $(dE/dx)_{eff} \sim 0.2\ (dE/dx)_{el}$ [9,31]. Many irradiation conditions were simulated by varying the track radii and initial temperature. Therefore, a large number of scenarios have been simulated, compared to the focused simulations in Ref. [25]. Our parametric study of track excitation allow us to compare results for several irradiation conditions (projectile/target combinations), but in the following, we will present mostly those cases that can be directly compared to relevant experimental data on polymer thin films.

The evolution of the system after the ion incidence was analyzed using the Open Visualization Tool (OVITO) [32] and followed for at least ~100 t_{LJ}. This time was enough to ensure that crater features had not changed size during the last stage of the simulation. However, this does not guarantee the lack of possible extremely slow thermal relaxation processes [33], but their effect should be small, given that the final temperature of the crater area was significantly below the melting temperature of the solid.

In order to model a thin film, the particles were artificially labeled as belonging to the film or the substrate according to their initial depth within the sample, and the track was heated only within the film thickness h. Thus, in our model system the film-substrate interface is made of the same material. As the total box size was the same for all simulations ($80 \times 80 \times 80 \times nm^3$), thinner films had thicker substrates and vice versa. The absence of a spike in the substrate means it is treated as a material where electronic excitations are relaxed before coupling to atomic motion. This is a reasonable assumption for crystalline Si [7], a common substrate in thin film experiments. Of course, at the film/substrate interface, exchange of energy implies that crater features might be influenced by the substrate. This turned out to be negligible except for ultrathin films ($h < 5$ nm) and very hot tracks (more than 20,000 K).

3. Results and discussions

(a) Particle ejection and cratering formation

Fig. 1 shows a 3D view of simulated craters for both amorphous and crystalline samples. The crater includes a large rim, as also seen in simulations of keV atomic [26] and cluster [34] ions, and larger projectiles [34,35]. Such similarities point to general formation processes involving atoms displaced by momentum transfer, phase transitions and plasticity. In the case of cluster bombardment of a LJ system [34], solid-vapor transition and melt flow [34,35] were found to contribute to crater formation, mostly due to a piston effect by the incident cluster, but here the liquid flow proceeds as a kind of "fountain effect", as described for collision cascades [36] and ion tracks [19]. For a cubic fcc crystal dense packing occurs along ⟨1 1 1⟩ directions and this is the most efficient direction for energy transport. Observed from the top of a (001) surface, as in Fig. 1a, this results in a highly plane-oriented crater rim with 4-fold symmetry. On the other hand, the amorphous solid does not contain any preferential orientation, thus the rim has a circular shape, in agreement with the cylindrical hot track.

Fig. 2 shows kinetic energy profiles for crystalline and amorphous samples, ~10 ps after the spike for a track radius of 3 nm. Top and side views are shown of a thin slice in the center of the impact point. Again, closed-packed ⟨1 1 1⟩ directions lead to faster energy transport, and the profiles display the resulting four-fold symmetry, given that we have a (001) surface, as mentioned above for the crater rim. The amorphous sample on the other hand, shows the expected circular expanding profile. The slower energy dissipation and cooling of the excited region in the amorphous sample is evident in Fig. 2. The very hot central region (labeled red[1], with mean particle energies above the vaporization temperature) and the molten region (colors from light blue to yellow) are both longer and wider in the amorphous films. Consequently, the molten region

[1] For interpretation of color in Fig. 2, the reader is referred to the web version of this article.

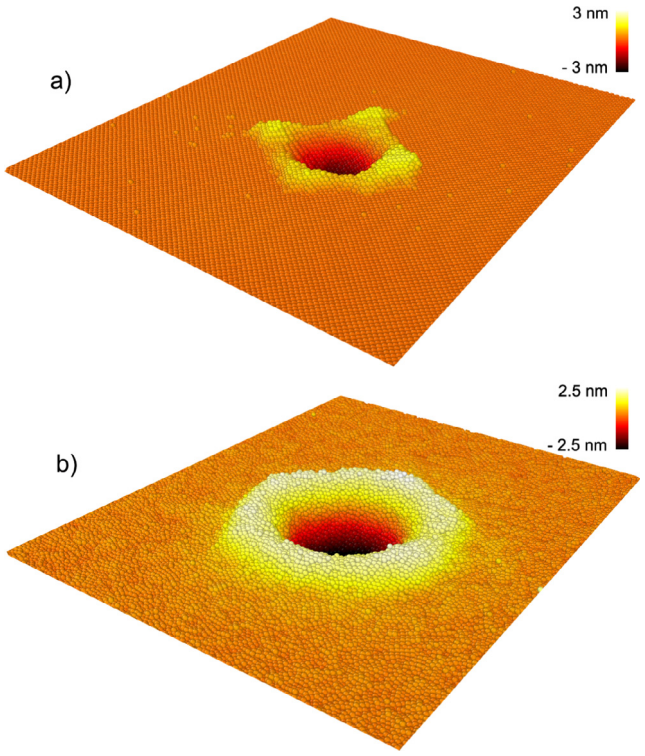

Fig. 1. 3D view of crystalline (a) and amorphous (b) samples at the end of the simulation for a thickness h = 10 nm, R_{track} = 2 nm and T^* = 25. Coloring depicts particle height, with brighter color indicating higher regions. The cubic crystalline geometry results in the 4-fold symmetry of the crater rim in the crystalline sample, while the round rim reflects the lack of preferential directions in the amorphous sample. (For interpretation of the references to colour in this figure legend, the reader is referred to the web version of this article.)

around the ion track is sustained for a longer time in the amorphous sample, leading to larger craters and rims due to substantial melt flow, as will be later discussed. Supplemental Fig. 1 shows a series of snapshots of the track evolution for 30 nm thick crystalline and amorphous films, where the dynamics of energy dissipation and crater formation can be seen in detail [37]. The slower energy dissipation in the amorphous films seen in the simulations is expected, because heat transfer in insulators takes place mainly due to lattice vibrations and the scattering of phonons is much more probable due to the disordered arrangement of atoms.

Fig. 3 exhibit a thin slice of an amorphous sample, with particles either colored by their displacement with respect to their original positions, or represented by the displacement vectors between those positions. Some isolated particles of course move to the surface due to focusons [38], but movies of the crater evolution show that these groups moved coherently, due to the pressure pulse produced by the track (see for instance Supplemental Movie 1 [37]). Typically, the first layer of the rim is composed of thin platelets pushed out by a pressure pulse, plus some liquid flow decorating the side and top of those platelets. Such platelets are similar to the ones resulting from cooperative atomic motion due to subsurface collision cascades [39]. This pressure effect occurs as predicted by the "pressure-pulse" model, successfully used for electronic sputtering of organic materials [40].

Regarding the role of plasticity, Fig. 4 compares defects remaining after cooling of the crystalline and amorphous samples. Defects have been filtered using the centrosymmetry parameter. There are a few vacancies (seen by the defective atoms surrounding them), a dislocation loop at the bottom of the crater, and a few interlocked stacking faults (SF). The low stacking fault energy of the LJ solid will lead, under large stress, mostly to partial dislocations with a SF behind [41]. Most partial dislocations and SFs recover and disappear after stress unloading, as the crater cools down. Their role in the final crater volume would be minimal, unlike what occurs for craters in fcc metals by large cluster bombardment [34,35]. Dislocation junctions might survive the cooling of the track, as in Fig. 4a, and in this case, immediately below the crater a void remain, as seen for the crystalline solid in Supplemental Fig. 1h [37]. This is similar to what is observed in nanoindentation simulations of fcc solids [42]. For the amorphous sample, small clusters of particles that have re-crystallized due to heating and stress are seen in Fig. 4b (in dark blue). Given their small sizes, their influence in the final crater dimensions should be negligible.

The pressure required to push a step out and contribute to the rim, or to create dislocations, could be estimated from a simple strength model. In the discussion below, all numbers are given in dimensionless LJ reduced units (length in units of σ = 0.5 nm, stress, pressure and moduli in units of $\varepsilon/\sigma^3 \sim 90$ MPa). Given a hemispherical feature like the crater, the stress to deform the surrounding material plastically is roughly $\sigma_p = Gb/2R$, where G is the shear modulus, R is the crater radius and b is the magnitude of the dislocation Burgers vector, of order 1. For a LJ crystal, G ~ 50 [43]. In the region where there is a rim, R ~ 10, and $\sigma_p \sim 2.5$ in the early stages. Energy density leads to an initial pressure of ~12, rapidly decaying due to energy loss by an outgoing shock wave and thermal conduction away from the track. Therefore, the stress required for plasticity is easily overcome by the pressure resulting from the track, which can still reach values of 4–6 in the region surrounding the track after 19–30 ps. In the region where the rim disappears, the pressure cannot be kept for long and does not reach high values after ~19 ps. For the amorphous LJ solid, a typical threshold for plasticity is given when the shear stress reaches values of ~1.5 [44], and the pressure is high enough to produce plastic deformation. Pressure might lead to shear transformation zones (STZ) [45], i.e. small clusters of particles that experience significant shear. STZ might in turn lead to shear bands [46]. Here evidence for STZs is observed, indicating clearly that the pressure was also high enough to produce plastic deformation. However, the small STZs do not join to form a shear band. In both crystalline and amorphous cases, the presence of defects after irradiation might lead to radiation-induced mechanical hardening, provided that defect kinetics at macroscopic times does not destroy them. This is a phenomenon studied for collision cascade irradiation [47], but not so much for irradiation in the electronic regime [48].

(b) Dependence on the effective energy loss

Fig. 5 shows quantitative data on the average crater diameter (D_{crater}), crater depth (Z_{crater}) and rim volume (V_{rim}) for crystalline and amorphous samples as a function of the effective energy loss. V_{rim} is the volume of the protruded region above the unperturbed surface position around the crater hole. The definitions of the crater dimensions are given in the insets of Fig. 5. The analyses were performed using tools available in OVITO. The error bars provided in the figure were estimated taking into account both statistical fluctuations among similar simulations (ran with different random seeds) and uncertainties in the measurements of the crater dimensions. Variations due to the simulations themselves are negligible compared to uncertainties in the crater size measurements. The later stems mainly from the difficulties of determining the exact point where a given feature begins or ends and the plane of reference for the unperturbed surface.

Craters are wider for the amorphous sample, but the crater diameter in both systems shows a square-root dependence with $(dE/dx)_{eff}$. This scaling is similar to what was obtained previously for a crystalline LJ solid [27]. Crater depth, on the other hand, first

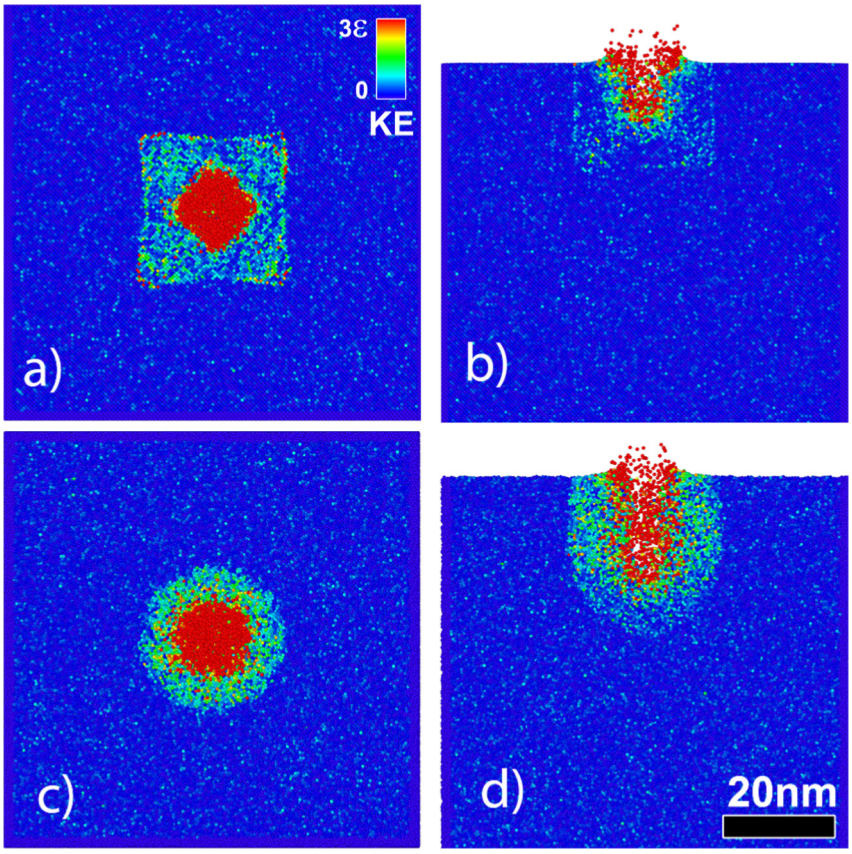

Fig. 2. Kinetic energy color maps for 20 nm thick crystalline (a and b) and amorphous (c and d) films 10 ps after the spike. Left column shows top view plots, while right column shows a side view at the center of the crater. The initial track radius is 3 nm and $T^* = 25$. The energy scale is given in terms of ε. Energy is preferentially propagated along nearest neighbor ⟨1 1 1⟩ directions in the crystalline sample, leading to fast and efficient energy dissipation.

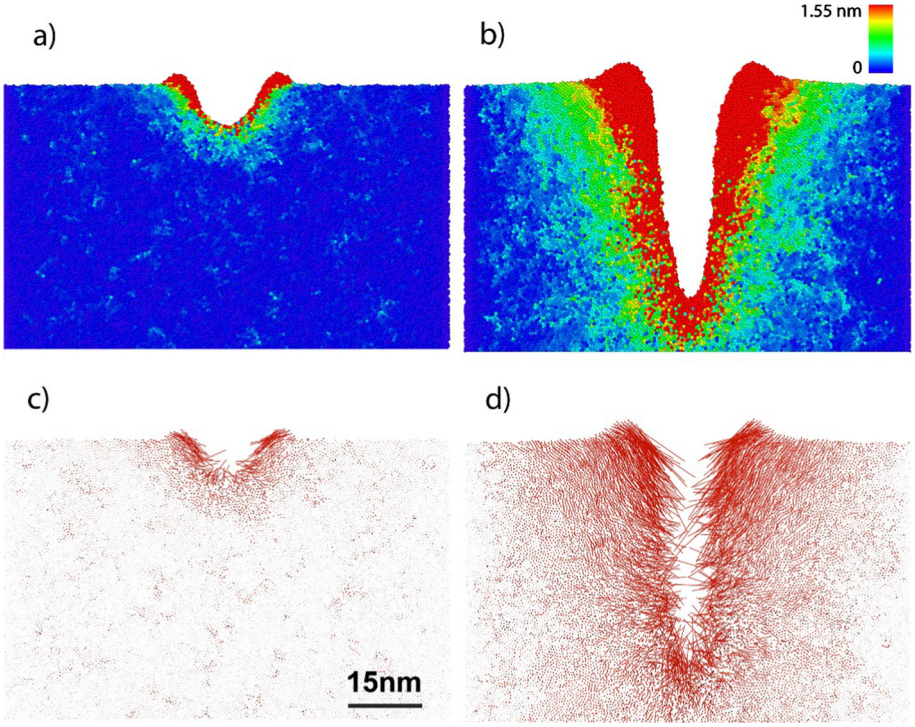

Fig. 3. Final (t = 190 ps) displacements and displacement vectors from original positions of particles around the ion impact site ($T^* = 25$, $R_{track} = 3$ nm) for amorphous films of h = 6.5 nm (a and c) and h = 43 nm (b and d). Color is coded by displacement magnitude. Red coloring starts when displacement is bigger than 2 lattice parameters for the crystalline sample. Vectors larger than a lattice parameter indicate melting/vaporization. Most of the sputtered particles and the top rim layers originate from regions which suffered a phase transition. (For interpretation of the references to colour in this figure legend, the reader is referred to the web version of this article.)

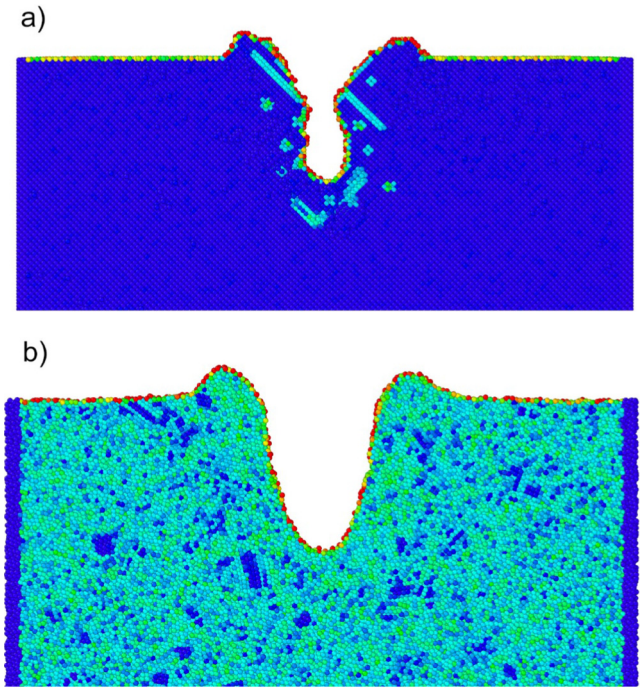

Fig. 4. Final snapshot (t = 190 ps) of a 20 nm thick film for an ion track of T* = 25 and R_{track} = 3 nm, showing "defective" regions. The slices of (a) crystalline and (b) amorphous samples are colored by centrosymmetry from 0 (perfect crystal, blue) to 4 (red). Defects are seen in the crystalline sample (stacking faults and point defects surrounding the crater, and a dislocation loop below the crater). There are a few recrystallized regions in the amorphous sample, observed as blue clusters. (For interpretation of the references to colour in this figure legend, the reader is referred to the web version of this article.)

increase sharply with increasing $(dE/dx)_{eff}$, but the dependence weakens as Z_{crater} approaches the thickness of the films. The depth of the crater reaches the physical limit of the film (i.e., Z_{crater} = h) at energy loss values close to 1 keV/nm in the amorphous films, while for the crystalline case larger $(dE/dx)_{eff}$ values are required. Thus, crater depth and radius do not scale equally with energy loss, in contrast to simple scaling laws that predict a roughly hemispherical crater, with each dimension proportional to $(dE/dx)^n$ (with n = 1/3 [35], 1/2 [16], or 1 [40]).

For the crystalline films, in several cases the fast cooling of the crater together with a dense dislocation network lead to the collapse of crater walls, which formed faceted voids below the crater (Supplemental Fig. 1h [37]). For one value of $(dE/dx)_{eff}$, the appearance of voids was particularly pronounced and a point was added in Fig. 5b, showing the value of the cavity depth including the length of the void. Further increase in energy loss did not result in deeper craters (we tested up to 3 keV/nm). This means that the initially non-excited particles of the substrate contribute negligibly to sputtering or to the crater shape. Diffusion of the excitation energy to the substrate is also very limited along the axis of the ion incidence, during the short time scale for cratering and sputtering. We further discuss substrate effects in section (c) below.

The rim volume is much larger for the amorphous sample, although, as for the crater hole, the scaling with $(dE/dx)_{eff}$ is similar for both systems. Curves of $V_{rim} \propto (dE/dx)^2_{eff}$ are shown as solid lines in Fig. 5c. The square dependence scaling is approximate, as it becomes weaker at larger dE/dx, especially for the amorphous case. It is also clear from Fig. 5c that there is a minimum or threshold stopping power for rim formation, which is phase dependent. The smallest effective energy loss to observe a distinguishable rim in the amorphous sample is close to 0.15 keV/nm, but in the

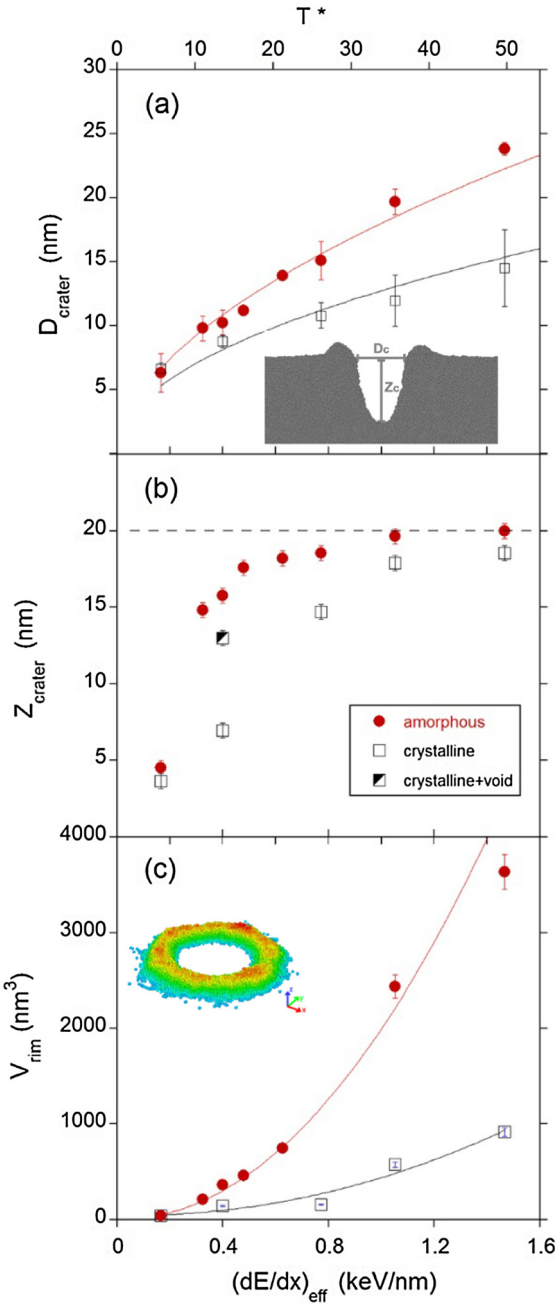

Fig. 5. Crater diameter D_{crater} (a), crater depth Z_{crater} (b), and rim volume V_{rim} (c) as function of effective stopping power for amorphous (circles) and crystalline (squares) films with h = 20 nm. The insets illustrate the variable definitions. Lines for crater diameter are $D_{crater} \sim (dE/dx)^{1/2}_{eff}$, as suggested in [27]. The crater depth curve includes a point where the size of the void below the "regular" crater was added to compute the total depth and a dashed line indicating the film thickness. Rim volume plots includes $(dE/dx)^2_{eff}$ fits (solid lines).

crystalline sample it is ~0.7 keV/nm. The lower threshold for the rim formation in the amorphous films is attributed to the lower stress threshold for plasticity in this system (critical stress of 1.5 versus 2.5 for the crystal, as previously discussed), and to the larger contribution of melt flow to the rim in the amorphous film. Melt flow has already been considered as an important mass transport mechanisms in simulations of cratering by keV and MeV ions of high dE/dx [34,35,26].

In summary, all crater dimensions tend to be larger in the amorphous targets. As the initial deposited energy is the same in both cases, such differences must be related to the way energy is dissi-

pated and transported out of the excited region after the ion passage. As already pointed out, this is in part due to the faster energy transport in the crystalline samples, where deposited energy is rapidly diluted in larger volumes. Free volume and particle mobility is also enhanced in the amorphous system, facilitating mass transport and melt flow out of the excited region during longer times after the ion excitation. Such differences in energy transport, which affects the "slower" events of crater formation and relaxation, are, however, not so important for the faster process involved in sputtering, as discussed below.

Fig. 6 shows the sputtering yield (Y) as a function of effective stopping power for amorphous and crystalline films of h = 20 nm. Both crystalline and amorphous targets present nearly identical sputtering yields. Unlike the predictions of quadratic dependence with dE/dx in analytical spike models [14], which neglect pressure and surface effects, the dependence observed here is roughly linear, same as in simulations of infinitely long tracks [21]. This is to be expected as far as most of the ejection depth is smaller than film thickness. The exit angle distribution of sputtered atoms at one fixed dE/dx is also shown in Fig. 6. The amount of ejected particles and the mean sputtering angle (33 ± 19°) were very similar in both systems, crystallinity having no influence in this matter. We attribute such similarity to the extremely high temperature and disordered condition of the track region from where most ejected particles originate, as indicated by the displacement arrows in Fig. 3.

The amount of sputtered particles in our simulations was significantly smaller than the number of particles corresponding to the crater volume, as already noted previously [21,27]. This is in part due to melt flow and redeposition at the crater rims of highly excited particles of the spike and to the particles that are pushed radially towards the walls of the crater, where they accommodate in a compacted region. Both effects are clearly seen in the movie provided in Supplemental material [37]. For thick films, the number of sputtered particles is 30–50% smaller than the number of particles in the rim.

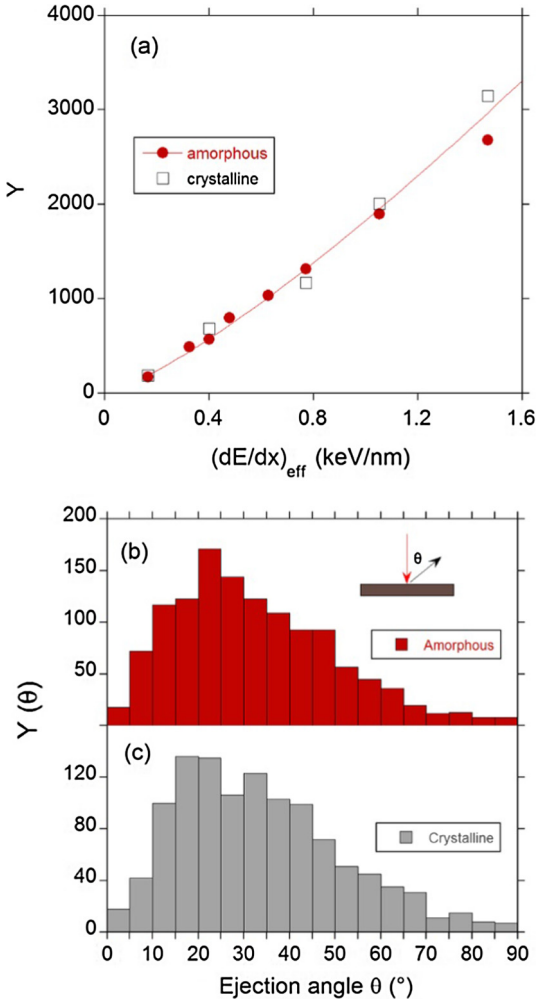

Fig. 6. Comparison of sputtering from amorphous and crystalline LJ films (h = 20 nm) for an excited track of R_{track} = 3 nm. (a) Yield of sputtered particles as function of effective stopping power for amorphous and crystalline films. A fit with a power of 1.2 is included, as suggested from simulations of infinitely long tracks [24] (b) Exit angle distribution of sputtered particles from crystalline and amorphous samples in the case of $(dE/dx)_{eff}$ = 0.77 keV/nm (T^* = 25). The average exit angle is very similar in both cases: 33 ± 19° for the crystalline films and 32 ± 19° for the amorphous, where the uncertainty is the standard deviation of the population. The standard error for the mean is ~0.5°.

(c) Thickness dependence

In this section, we discuss how surface effects change with decreasing film thickness. For this set of simulations, LJ amorphous samples were excited by a spike with T^* = 25 and an initial radius of 3 nm. Compared to the scenario for thick films described in section (a), for thinner films both the pressure pulse and melt flow are reduced, and cratering/sputtering is mostly due to rapid phase explosion, as for bombardment of large clusters [34]. Fig. 7 shows top-view pictures of MD craters for different film thicknesses *h* together with AFM images of experimental craters seen on (amorphous) PMMA films [25] bombarded by 923 MeV Pb ions [$(dE/dx)_{el}$ close to 15 keV/nm]. We also added in Fig. 7 images of craters in crystalline films of different thickness, but these simulations were run with R_{track} = 2 nm. The lateral sizes of craters in the amorphous LJ films and PMMA films are remarkably similar. We note that AFM images of such nanometer-sized features suffer from tip convolution effects. This tends to widen protruded regions and limits the depth of narrow holes that can be probed, especially for very deep cavities. Crater diameters are not much affected by tip effects, provided that high quality tips are used [7]. In the following, we concentrate our discussion on the amorphous LJ case that has a morphology very similar to the experimental craters in polymer films.

Under the conditions described above, MD crater diameters in the amorphous films are similar (~25% smaller) to those measured experimentally. However, MD rim volumes and crater depths are substantially larger than experimental ones, reflecting the much weaker bonding of a LJ system, compared to entangled polymer chains of real films. For example, simulated rim volumes are a factor of four larger. Despite such quantitative disagreement (expected in such a simple model), the simulations mimic very well the dependence of crater diameter and rim volume with thickness seen in the experiments. Starting from a saturation value at thick layers, the rim size remains unchanged down to a thickness of ~30 nm, followed by a steep decrease for thinner layers. A similar condition is observed for the thickness dependence of the craters radii, but the critical thickness below which thickness-dependent effects start is shifted to approximately h < 10 nm, and the shrinking of the crater hole with *h* is less pronounced, as in the experiments [25]. In the simulations, the pressure pulse is weaker and cooling of the excited track is more efficient in short tracks, both contributing to the decreased radiation damage efficiency on ultrathin layers. This decrease in crater and rim dimensions is also in accordance with theoretical predictions of models for which radiation effects at the surface are driven by the sum of elementary excitations along the track [40,25]. Such cooperative action becomes naturally weaker for shorter track lengths. Long-range effects along the track are particularly critical

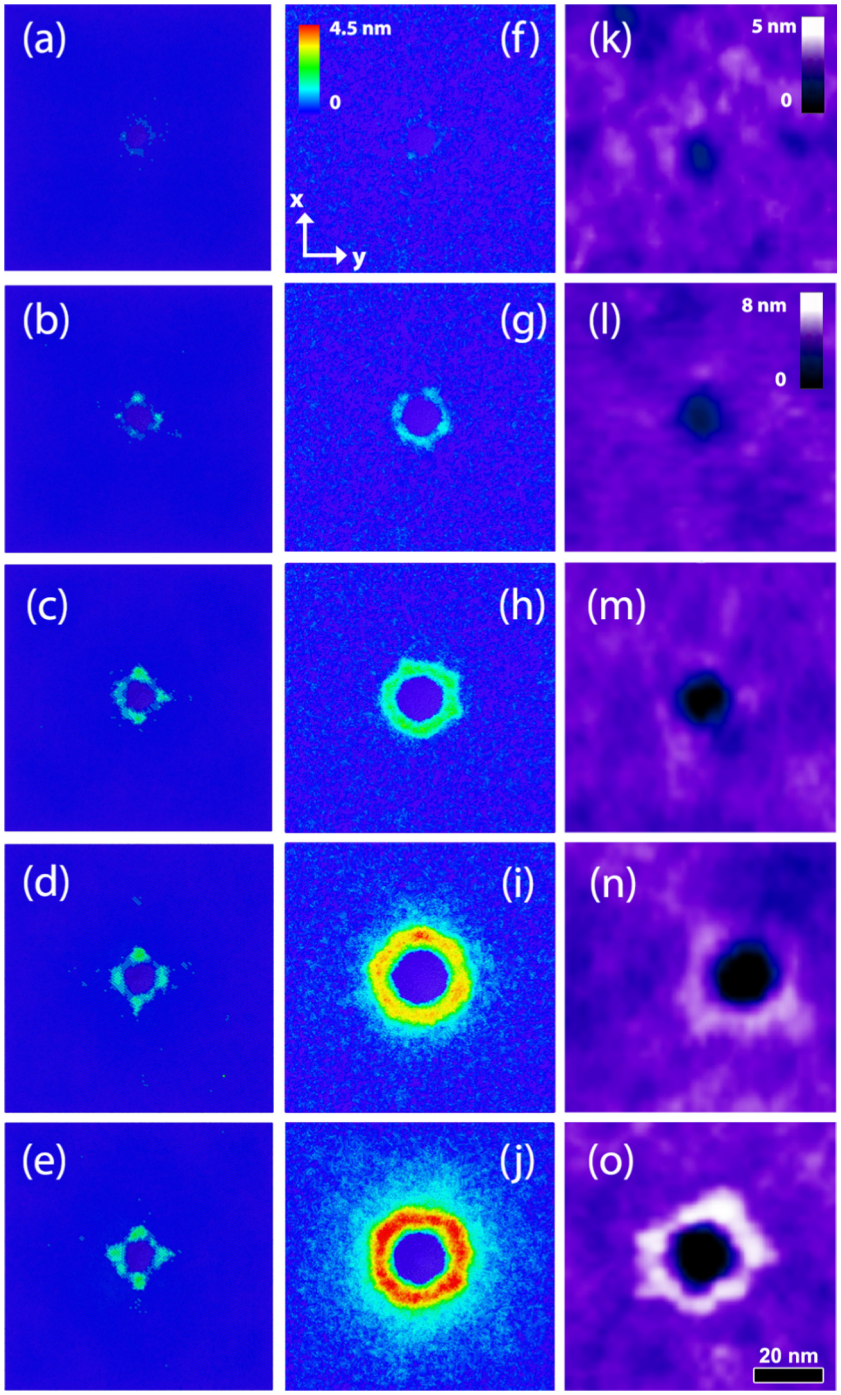

Fig. 7. Comparison of experimental craters produced by swift heavy ions in PMMA with simulated craters in crystalline and amorphous LJ films. Top view, AFM-like images of simulated craters ($T^* = 25$, $R = 3$ nm) for (a–e) crystalline and (f–j) amorphous films of different thicknesses: (a) 2.5 nm; (b) 3.5 nm; (c) 8.5 nm; (d) 18.5 nm; (e) 43.5 nm; (f) 2 nm; (g) 3.6 nm; (h) 6.6 nm; (i) 20 nm; (j) 43 nm. Right row depicts (k–o) AFM images of craters produced by 923 MeV Pb in PMMA thin films of thicknesses (k) 2 nm; (l) 4 nm; (m) 8 nm; (n) 20 nm (o) 42 nm. The images size is 80×80 nm^2 for all cases.

to the rim formation in the simulations, because its formation is partly due to lifted surface platelets, requiring a coordinated push from deep regions. This is consistent with the larger critical thickness observed for the rim volumes.

There are also some important aspects to note concerning the dependence of crater depth with thickness. The depth of simulated craters in amorphous LJ films is equal to the film thickness ($Z_{crater} = h$) for h values up to ~30 nm. Even for the thickest film simulated (60 nm), crater depth is far from reaching a saturation value. In the experiments, however, crater depth does not follow the curve $Z_{crater} = h$ even for small h, and the maximum crater depth is reached at h ~ 20 nm [25]. Simulated craters are deeper, not because of sputtered particles, but due to the large contribution of melt flow from deep layers in a LJ material. As seen in Fig. 3d, many hot particles move upwards from the inner regions of the track and are deposited at the rim region. In fact, in the simulations, the sputtering yield is dominated by particles originally lying above $z = h/2$ (with z = 0 defined as the surface position), even in very thin films. Fig. 8 shows the distribution of the depth of origin of ejected particles from films of two different thickness (2 and

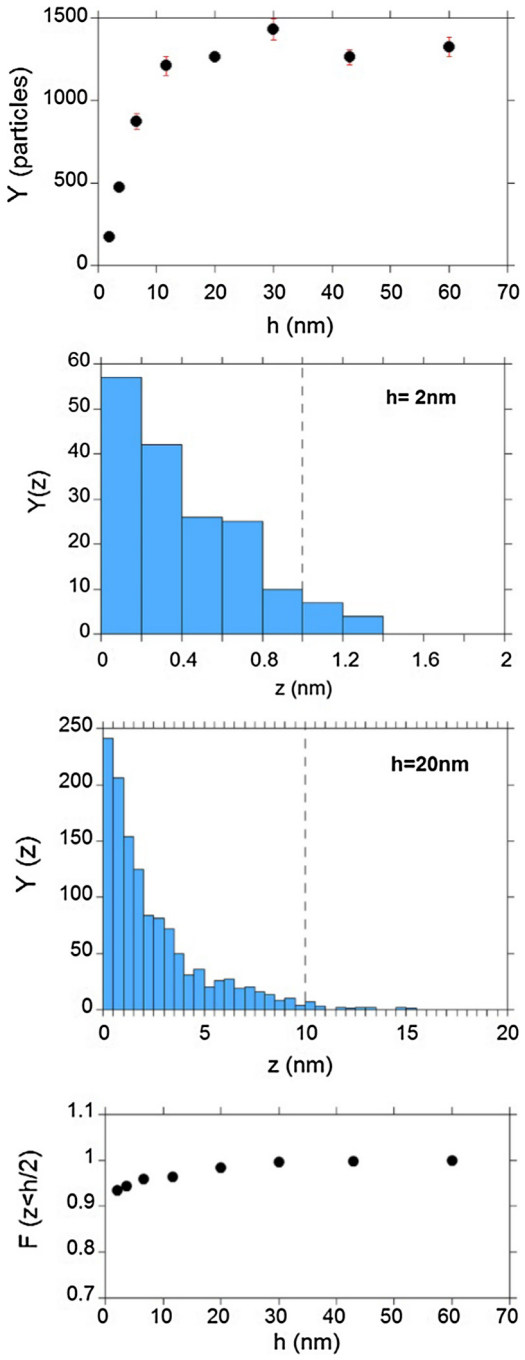

Fig. 8. Sputtering yield and depth of origin of ejected particles as a function of h. (a) Total sputtering yield as a function of thickness for R = 3 nm and T* = 25. (b and c) Distribution of the number of puttered particles as a function of the depth of origin z for a 2 nm and a 20 nm thick films. (d) Fraction of ejected particles originating from depths $z < h/2$ for various film thicknesses.

20 nm), and the fraction of ejected particles originating from $z < h/2$ for all thickness tested. For the 2 nm film, ~94% of the ejected particles comes from $z < h/2$. For thicker films, this fraction is even larger. As a consequence, total sputtering yield drops below a critical thickness [Fig. 8a], which is related to the maximum depth of origin of ejected particles (~10 nm) in thick films and not to the maximum crater depth. The angular distribution of ejected particles, on the other hand, is not much affected by thickness reduction.

The h/2-limitation for the depth of origin of ejected particles from thin films can be understood noting that momentum transfer is critical for particle ejection. In the simulations, the z-component of the velocity of excited particles tends to point toward the surface only for particles located at a position with $z < h/2$. This is clearly seen in Fig. 3c and d, where displacement vectors from initial positions have upward arrows starting near $z = h/2$. Below that depth, displacements have a high degree of randomness, or tend to point downwards. Such observations are also in agreement with predictions by analytical models based on sum of impulses [18,40]. Due to symmetry and neglecting substrate contributions, the total impulse transmitted to a particle in a film points upward only if it is located at a position with $z < h/2$. At points with $z > h/2$ the impulse direction is inverted and push particles towards the substrate.

The fact that many experimental trends with PMMA/Si films are reproduced with the simple LJ film/substrate model used here, implies that crystalline Si in the experiments acts to a good approximation as a non-excitable substrate, as in the simulations (this may not be the case for amorphous Si, however [49]). We already pointed out that exchange of energy between particles at the bottom of the track and the initially non-excited particles is small. Our results are thus compatible with excitation decay occurring rapidly and over short distances and substrate effects, if any, would only be relevant for the thinnest films considered here.

Here we employed a very simple model of particles interacting via LJ potentials in tracks of variable length to simulate cratering in thin films of organic materials. Generating and irradiating large samples (>10^6 particles) with polymer chains simulated by more complex interactions, like the Brenner's or ReaxFF potentials [50,51], is an obvious improvement to simulate a "real" polymer film in future work. Other simulation configurations that better model the role of the substrate can also be employed, including using a 2-type LJ system to mimic different mechanical properties of film and substrate or adding electronic heating for insulating substrates with different temperature and heating times. This will for sure improve quantitative agreement with cratering features in real experiments.

4. Conclusions

Impacts of energetic heavy ions at the electronic energy loss regime were simulated to study cratering and sputtering in organic thin films of variable thicknesses. We have employed a simple model material with particles interacting via the LJ potential and arranged in crystalline and amorphous phases. In both cases, crater formation is controlled by track size and temperature, with crater size being mostly determined by evaporation and melt flow from the hot track, and the rim size by melt flow and by coherent displacement of excited particles. Craters and rims, however, are much larger in amorphous films essentially due to the slower cooling of the excited region and the larger free volume, which facilitates mass transport and melt flow out of the excited region during longer times after the ion excitation. On the other hand, sputtering yields from both crystalline and amorphous samples are similar (including the angular dependence), indicating that ejected particles arose mostly from nascent events from the highly excited track, making the initial phase structure of the material not relevant. We also found a large dependence of the induced surface effects on film thickness below a critical thickness value. The decreased radiation damage efficiency on ultrathin layers is related to the more efficient cooling of shorter tracks and weakening of additive excitation events from deep layers (pressure pulse). Several important features observed in experiments with cratering in polymer thin films were reasonably reproduced in amorphous LJ samples, showing the usefulness of simple interaction potentials to simulate complex organic materials perturbed by high-energy ions.

Acknowledgements

We thank discussions with R. Gonzales-Valdez, V. de Menezes, and D. Tramontina, E.M.B. Expresses thanks for support from SeCTyP-UNCuyo under Grant No. M003, and ANPCyT under Grant No. PICT-2014-0696. This work is part of the IAEA Coordinated Research Project on *Development of Molecular Concentration Mapping Techniques using MeV focused ion beams*, CRP F11019 (Contracts 18352/R0 and 18686). CAPES and CNPq are also acknowledged for financial support.

Appendix A. Supplementary material

Supplementary data associated with this article can be found, in the online version, at http://dx.doi.org/10.1016/j.commatsci.2016.12.001.

References

[1] A. Meftah, F. Brisard, J.M. Costantini, E. Dooryhee, M. Hage-Ali, M. Hervieu, Phys. Rev. B 49 (1994) 12457, http://dx.doi.org/10.1103/PhysRevB.49.12457.
[2] M. Toulemonde, W. Assmann, C. Dufour, A. Meftah, C. Trautmann, Nucl. Instrum. Methods Phys. Res. B 277 (2012), http://dx.doi.org/10.1016/j.nimb.2011.12.045.
[3] R.L. Fleischer, P.B. Price, R.M. Walker, in: Nuclear Tracks in Solids: Principles and Applications, University of California Press, 1975.
[4] M. Toulemonde, W. Assmann, C. Trautmann, F. Grüner, Phys. Rev. Lett. 88 (2002) 057602, http://dx.doi.org/10.1103/PhysRevLett. 88.057602.
[5] R.D. Macfarlane, D.F. Torgerson, Phys. Rev. Lett. 36 (1976) 486, http://dx.doi.org/10.1103/PhysRevLett. 36.486.
[6] H. Dammak, A. Dunlop, D. Lesueur, Philos. Mag. A 79 (1999) 147, http://dx.doi.org/10.1080/01418619908214280.
[7] R.M. Papaléo, M.R. Silva, R. Leal, P.L. Grande, M. Roth, B. Schattat, G. Schiwietz, Phys. Rev. Lett. 101 (2008) 167601, http://dx.doi.org/10.1103/PhysRevLett.101.167601.
[8] J. Kopniczky, C.T. Reimann, A. Hallén, B.U.R. Sundqvist, P. Tengvall, R. Erlandsson, Phys. Rev. B 49 (1994) 625, http://dx.doi.org/10.1103/PhysRevB.49.625.
[9] D. Schwen, E. Bringa, J. Krauser, A. Weidinger, C. Trautmann, H. Hofsäss, Appl. Phys. Lett. 101 (2012) 113115, http://dx.doi.org/10.1063/1.4752455.
[10] R.M. Papaléo, L.S. Farenzena, M.A. de Araújo, R.P. Livi, M. Alurralde, G. Bermudez, Nucl. Instrum. Methods Phys. Res. B 148 (1999) 126, http://dx.doi.org/10.1016/S0168-583X(98)00877-5.
[11] O. Ochedowski et al., Nat. Commun. 5 (2014), http://dx.doi.org/10.1038/ncomms4913.
[12] H.M. Urbassek, Nucl. Instrum. Methods Phys. Res. B 122 (1997) 427, http://dx.doi.org/10.1016/S0168-583X(96)00681-7.
[13] R.E. Johnson, R. Evatt, Radiat. Eff. 52 (1980) 187, http://dx.doi.org/10.1080/00337578008210031.
[14] P. Sigmund, C. Claussen, J. Appl. Phys. 52 (1981) 990, http://dx.doi.org/10.1063/1.328790.
[15] G. Szenes, K. Havancsák, V. Skuratov, P. Hanák, L. Zsoldos, T. Ungár, Nucl. Instrum. Methods Phys. Res. B 166 (2000) 933, http://dx.doi.org/10.1016/S0168-583X(99)00733-8.
[16] I.S. Bitensky, E.S. Parilis, Nucl. Instrum. Methods Phys. Res. B 21 (1987) 26, http://dx.doi.org/10.1016/0168-583X(87)90135-2.
[17] L.E. Seiberling, J.E. Griffith, T.A. Tombrello, Radiat. Eff. 52 (1980) 201, http://dx.doi.org/10.1080/00337578008210033.
[18] D. Fenyö, R.E. Johnson, Phys. Rev. B 46 (1992) 5090, http://dx.doi.org/10.1103/PhysRevB.46.5090.
[19] M.M. Jakas, E.M. Bringa, R.E. Johnson, Phys. Rev. B 65 (2002) 165425, http://dx.doi.org/10.1103/PhysRevB.65.165425.
[20] P. Kluth, C.S. Schnohr, O.H. Pakarinen, F. Djurabekova, et al., Phys. Rev. Lett. 101 (2008) 175503, http://dx.doi.org/10.1103/PhysRevLett. 101.175503.
[21] E.M. Bringa, R.E. Johnson, M. Jakas, Phys. Rev. B 60 (1999) 15107, http://dx.doi.org/10.1103/PhysRevB.60.15107.
[22] R. Devanathan, P. Durham, J. Du, L.R. Corrales, E.M. Bringa, Nucl. Instrum. Methods Phys. Res. B 255 (2007) 172, http://dx.doi.org/10.1016/j.nimb.2006.11.021.
[23] O.H. Pakarinen, F. Djurabekova, K. Nordlund, P. Kluth, M.C. Ridgway, Nucl. Instrum. Methods Phys. Res. B 267 (2009) 1456, http://dx.doi.org/10.1016/j.nimb.2009.01.071.
[24] E.M. Bringa, R.E. Johnson, Surf. Sci. 451 (2000) 108, http://dx.doi.org/10.1016/S0039-6028(00)00015-7.
[25] R.M. Papaléo, R. Thomaz, L.I. Gutierres, V.M. de Menezes, D. Severin, C. Trautmann, et al., Phys. Rev. Lett. 114 (2015) 118302, http://dx.doi.org/10.1103/PhysRevLett. 114.118302.
[26] E.M. Bringa, K. Nordlund, J. Keinonen, Phys. Rev. B 64 (2001) 235426, http://dx.doi.org/10.1103/PhysRevB.64.235426.
[27] E.M. Bringa, R.E. Johnson, R.M. Papaléo, Phys. Rev. B 65 (2002) 094113, http://dx.doi.org/10.1103/PhysRevB.65.094113.
[28] E.M. Bringa, R.E. Johnson, Nucl. Instrum. Methods Phys. Res. B 193 (2002) 365, http://dx.doi.org/10.1016/S0168-583X(02)00806-6.
[29] S. Plimpton, J. Comput. Phys. 117 (1995) 1, http://dx.doi.org/10.1006/jcph.1995.1039.
[30] E.M. Bringa, R.E. Johnson, Nucl. Instrum. Methods Phys. Res. B 143 (1998) 513, http://dx.doi.org/10.1016/S0168-583X(98)00405-4.
[31] G. Szenes, Nucl. Instrum. Methods Phys. Res. B 116 (1996) 141, http://dx.doi.org/10.1016/0168-583X(96)00025-0.
[32] S. Alexander, Model. Simul. Mater. Sci. Eng. 18 (2010) 015012.
[33] R.M. Papaléo, R. Leal, W.H. Carreira, L.G. Barbosa, I. Bello, A. Bulla, Phys. Rev. B 74 (2006) 094203, http://dx.doi.org/10.1103/PhysRevB.74.094203.
[34] C. Anders, E.M. Bringa, F.D. Fioretti, G. Ziegenhain, H.M. Urbassek, Phys. Rev. B 85 (2012) 235440, http://dx.doi.org/10.1103/PhysRevB.85.235440.
[35] C. Anders, E.M. Bringa, G. Ziegenhain, G.A. Graham, J.F. Hansen, N. Park, et al., Phys. Rev. Lett. 108 (2012) 027601, http://dx.doi.org/10.1103/PhysRevLett.108.027601.
[36] M. Ghaly, R.S. Averback, Phys. Rev. Lett. 72 (1994) 364, http://dx.doi.org/10.1103/PhysRevLett. 72.364.
[37] "See Supplemental material at http://dx.doi.org/10.1016/j.commatsci.2016.12.001 for further details on the crater evolution for the molecular dynamics simulations of crystalline and amorphous samples".
[38] E.M. Bringa, R.E. Johnson, Dutkiewicz, Nucl. Instrum. Methods Phys. Res. B 152 (1999) 267, http://dx.doi.org/10.1103/PhysRevB.60.15107.
[39] K. Nordlund, J. Keinonen, M. Ghaly, R.S. Averback, Nature 398 (1999) 49, http://dx.doi.org/10.1038/17983.
[40] R.E. Johnson, B.U.R. Sundqvist, A. Hedin, D. Fenyö, Phys. Rev. B 40 (1989) 49, http://dx.doi.org/10.1103/PhysRevB.40.49.
[41] J.E. Hammerberg, T.C. Germann, B.L. Holian, R. Ravelo, Mat. Trans. A 35 (2004) 2609, http://dx.doi.org/10.1007/s11661-004-0220-7.
[42] Y. Gao, C.J. Ruestes, D.R. Tramontina, H.M. Urbassek, J. Mech. Phys. Solids 75 (2015) 58, http://dx.doi.org/10.1016/j.jmps.2014.11.005.
[43] D.J. Quesnel, D.S. Rimai, L.P. DeMejo, Phys. Rev. B 48 (1993) 6795, http://dx.doi.org/10.1103/PhysRevB.48.6795.
[44] P. Cao, X. Lin, H.S. Park, J. Mech. Phys. Solids 68 (2014) 239, http://dx.doi.org/10.1016/j.jmps.2014.04.004.
[45] C.A. Schuh, C. Lund, Nat. Mater. 2 (2003) 449, http://dx.doi.org/10.1038/nmat918.
[46] F. Shimizu, S. Ogata, J. Li, Acta Mater. 54 (2006) 4293, http://dx.doi.org/10.1016/j.actamat.2006.05.024.
[47] T. Diaz de la Rubia et al., Nature 406 (2000) 871, http://dx.doi.org/10.1038/35022544.
[48] S. Charnvanichborikarn, S.M.A. Worsley, S.J. Shin, S.O. Kucheyev, Carbon 57 (2013) 310, http://dx.doi.org/10.1016/j.carbon.2013.01.078.
[49] T. Bierschenk, R. Giulian, B. Afra, M.D. Rodriguez, et al., Phys. Rev. B 88 (2013) 174111, http://dx.doi.org/10.1103/PhysRevB.88.174111.
[50] K. Kremer, G.S. Grest, J. Chem. Phys. 92 (1990) 5057, http://dx.doi.org/10.1063/1.458541.
[51] A.C.T. van Duin, S. Dasgupta, F. Lorant, W.A. Goddard, Phys. Chem. A 105 (2001) 41, http://dx.doi.org/10.1021/jp004368u.